Supplement of Atmos. Chem. Phys., 26, 95–115, 2026
https://doi.org/10.5194/acp-26-95-2026-supplement

Atmospheric Chemistry and Physics
Open Access
EGU

Supplement of

Resolving the roles of soot and dust in cirrus cloud ice formation at regional and global scales: insights from parcel and climate modeling

Xiaohan Li et al.

Correspondence to: Xiaohan Li (xiaohanl@princeton.edu) and Songmiao Fan (songmiao.fan@noaa.gov)

S1 Parameterization of nucleation and ice growth processes in the parcel model

In our parcel model, homogeneous ice nucleation is parameterized following Koop et al. (2000). Heterogeneous ice nucleation is represented using deposition nucleation parameterizations from Ullrich et al. (2017, 2019) and immersion freezing parameterizations for dust from Alpert and Knopf (2016). Ice crystal growth follows Pruppacher et al. (1998), and the ice-nucleating active surface site (INAS) formulation is adopted from Ullrich et al. (2017). The explicit expressions for these parameterizations are summarized below.

S1.1 Homogeneous nucleation.

We follow the water-activity-based parameterization of Koop et al. (2000). The homogeneous nucleation rate J_{hom} (in $\text{cm}^{-3}\text{s}^{-1}$) is calculated as a function of the difference in water activity, Δa_w.

The nucleation rate J_{hom} is given by the polynomial fit:

$$\log_{10}(J_{\text{hom}}) = -906.7 + 8502(\Delta a_w) - 26924(\Delta a_w)^2 + 29180(\Delta a_w)^3 \tag{S1}$$

Where Δa_w is the difference between the water activity of the aqueous solution (a_w, which is assumed to be in equilibrium with the environment) and the water activity at the ice melting point ($a_{i,w}$):

$$\Delta a_w = a_w - a_{i,w} \tag{S2}$$

S1.2 INAS density parameterization for heterogeneous deposition nucleation

We use the ice nucleation active site (INAS) density parameterization framework from Ullrich et al. (2017). As shown in Equation 1, the number of ice crystals nucleated, N_i, is calculated based on the available aerosol surface area, S_{aer}, and the INAS density, $n_s(T, S_i)$, which is a function of temperature (T) and ice saturation ratio (S_i). The n_s parameterizations differ for each nucleation mode and aerosol type.

(a) Deposition nucleation (mineral dust). For deposition nucleation on mineral dust, n_s (in m^{-2}) is described by the "U-shaped" function of T (in K) and S_i:

$$n_s(T, S_i) = \exp\left\{\alpha(S_i - 1)^{1/4}\cos[\beta(T - \gamma)]^2 \frac{\text{arccot}[\kappa(T - \lambda)]}{\pi}\right\} \tag{S3}$$

The fit parameters for mineral dust (from Ullrich et al. (2017)) are: $\alpha = 285.692$, $\beta = 0.017$, $\gamma = 256.692$ K, $\kappa = 0.080$ K^{-1}, and $\lambda = 200.745$ K. This parameterization is valid for temperatures between 206 K and 240 K.

(b) Deposition nucleation (soot). For deposition nucleation on soot, the same functional form (Equation S3) is used. For soot with an organic carbon content of less than or equal 20 wt%, the fit parameters are: $\alpha = 46.021$, $\beta = 0.011$, $\gamma = 248.560$ K, $\kappa = 0.148$ K^{-1}, and $\lambda = 237.570$ K. This parameterization is valid for temperatures between 195 K and 235 K. However, the fit parameters $(\alpha, \beta, \gamma, \kappa, \lambda)$ are also dependent on the soot's organic carbon content, leading to a shift toward higher S_i for soot with higher organic carbon content as detailed in Ullrich et al. (2017).

(c) Scaling for coated aerosols. To account for the suppression of nucleation efficiency by coatings (e.g., sulfate or organics), we apply scaling factors based on Ullrich et al. (2019). The INAS density (n_s) from the parameterizations above is multiplied by a factor to represent this effect. Based on their findings, the n_s for coated mineral dust is scaled by a factor of 0.05, and for coated soot by a factor of 0.01.

S1.3 Immersion freezing (mineral dust)

For immersion freezing of mineral dust, we follow the stochastic, water activity-based immersion freezing model (ABIFM) framework developed by Alpert and Knopf (2016), which accounts for the time-dependent, stochastic nature of immersion freezing. This approach calculates the heterogeneous ice nucleation rate coefficient, $J_{het}(T, a_w)$ (in $\text{cm}^{-2}\text{s}^{-1}$), based on

classical nucleation theory, where the number of ice crystals (N_i) for an aerosol population with surface area S_{aer} and aerosol number N_{aer} is given by:

$$N_i = N_{aer}(1 - \exp(-J_{het} \cdot S_{aer} t)) \tag{S4}$$

The nucleation rate J_{het} is parameterized as a function of temperature T and water activity a_{w} as

$$\log_{10}(J_{het}) = m[a_{\mathrm{w}}(T) - a_{\mathrm{w,\,ice}}(T)] + c \tag{S5}$$

and

$$a_{\mathrm{w,\,ice}}(T) = p_{\mathrm{ice}}(T)/p_{\mathrm{w}}(T) \tag{S6}$$

where $p_{\mathrm{ice}}(T)$ and $p_{\mathrm{w}}(T)$ are the saturation water vapor pressure of ice and pure liquid water at temperature T. The parameters of $m = 22.62$ and $c = -1.35$ are used for natural dust.

S1.4 Ice crystal growth

The diffusional growth of an individual ice crystal (mass m_i) is calculated based on the standard equation for vapor diffusion and heat conduction, as found in Pruppacher et al. (1998):

$$\frac{dm_i}{dt} = \frac{4\pi C_i(S_i - 1)}{F_d + F_k} \tag{S7}$$

where C_i is the capacitance of the ice crystal, which accounts for its non-spherical shape; S_i is the ice saturation ratio of the environment; F_d and F_k are the "thermodynamic" (heat conduction) and "diffusion" (vapor diffusion) resistance terms, and

$$F_d = \frac{L_s}{K_a T}\left(\frac{L_s}{R_v T} - 1\right) \tag{S8}$$

$$F_k = \frac{R_v T}{D_v p_{s,i}} \tag{S9}$$

where L_s is the latent heat of sublimation; K_a is the thermal conductivity of air; T is the ambient temperature; R_v is the gas constant for water vapor; D_v is the diffusivity of water vapor in air; $p_{s,i}$ is the saturation vapor pressure over ice.

Table S1. Summary of parameters examined for the cirrus parcel model.

Parameter	**Unit**	**Values and binning**
Pressure (P)	hPa	100, 200, 300, 400
Temperature (T)	K	190 to 233, linear, step = 3 K
Updraft velocity	cm s^{-1}	0.1 , then log-spaced from 1 to 30 (20 values), log-spaced from 30 to 100 (20 values)
Dust mass concentration	ng m^{-3}	1 , then log-spaced from 10 to 10,000 (15 values)
Soot mass concentration	ng m^{-3}	1 , then log-spaced from 10 to 10,000 (15 values)
Sulfate mass concentration	μg m^{-3}	0.01, 0.1, 1
Sea salt mass concentration	μg m^{-3}	0.01, 0.1, 1

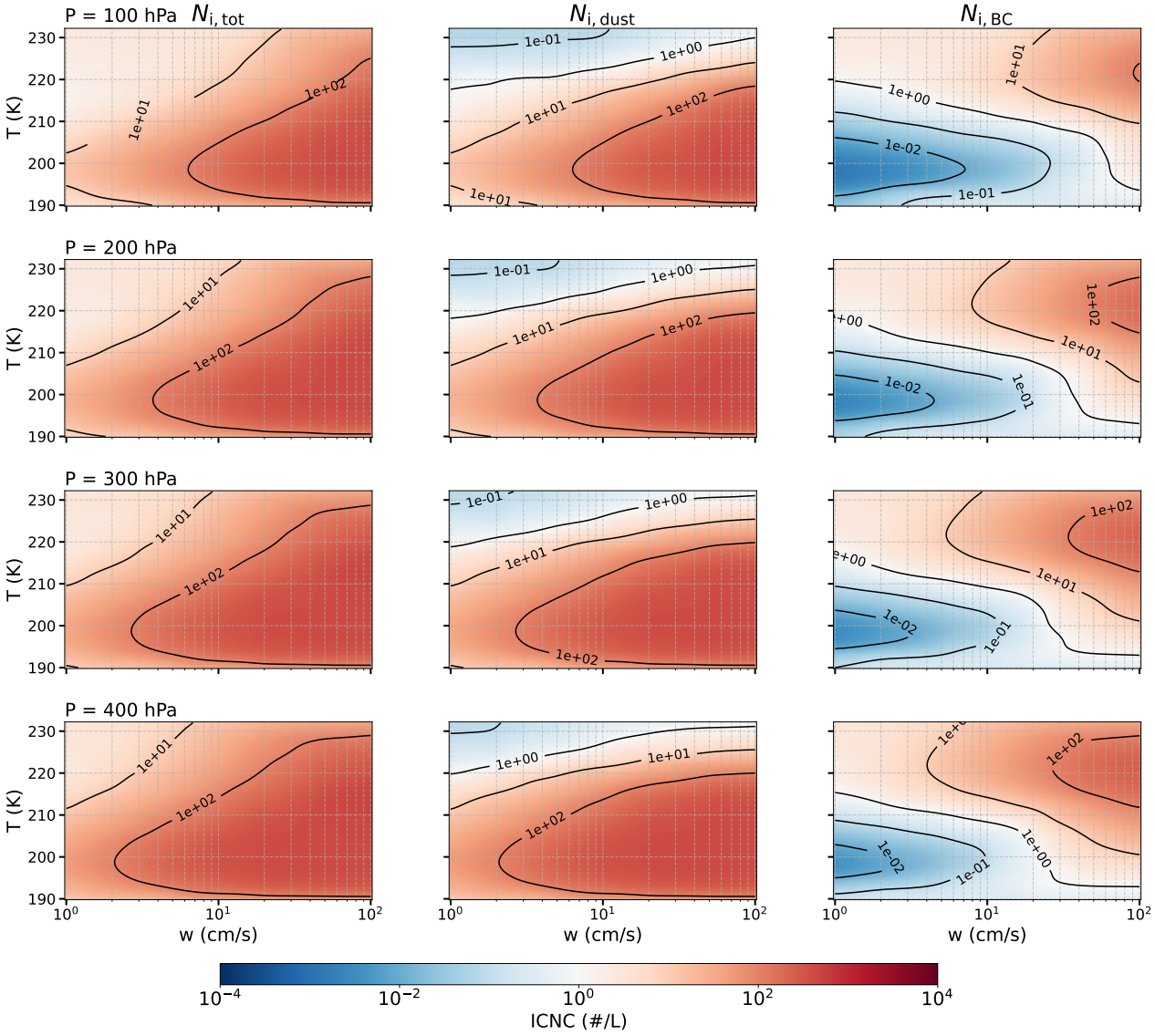

Figure S1. Total ice crystal number concentration ($N_{i,\mathrm{tot}}$) and ice contributions from dust ($N_{i,\mathrm{dust}}$) and black carbon (BC; $N_{i,\mathrm{BC}}$) The figure maps ICNC as a function of cloud base temperature (T) and updraft velocity (w). The columns separate the total concentration from its dust and BC components, allowing for a direct comparison of their activity. The rows illustrate how these relationships change with decreasing altitude (increasing pressure from 100 to 400 hPa), highlighting the different temperature and updraft regimes where each nucleation pathway becomes dominant and how this dominance is modulated by the ambient pressure. All simulations shown were performed with fixed mass concentrations of 100 ng m^{-3} for both dust and black carbon (BC), and background concentrations of 0.1 μg m^{-3} for both sea salt and sulfate.

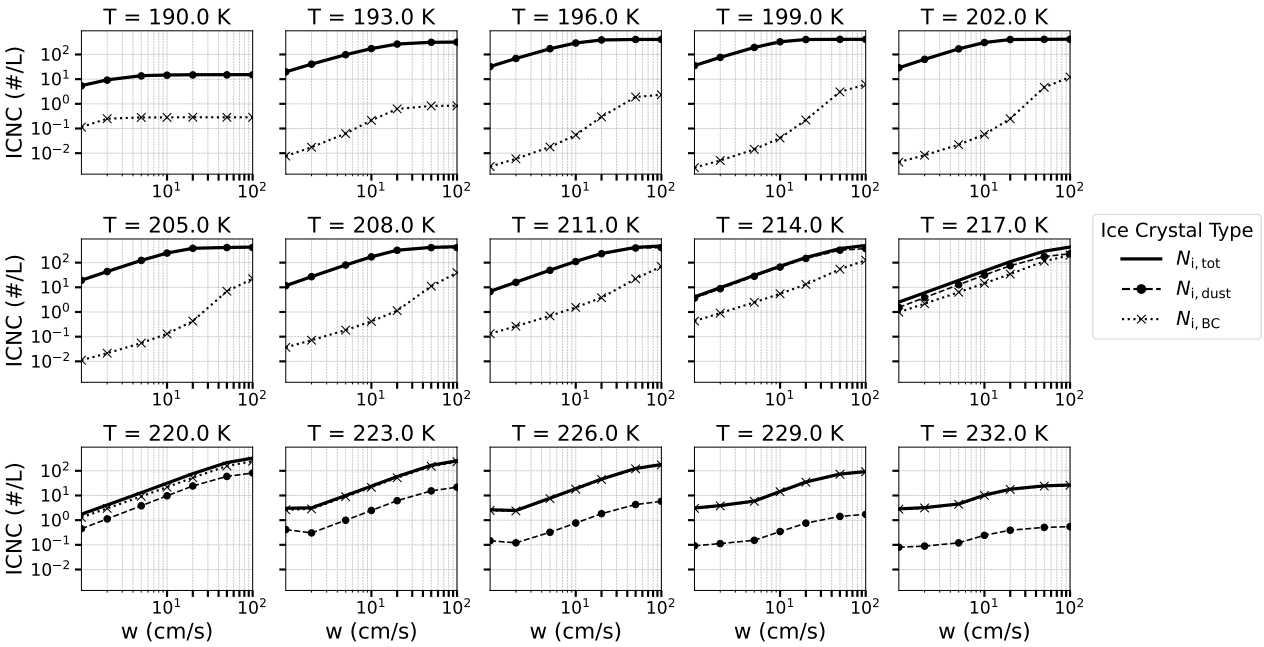

Figure S2. ICNC as a function of w. Each panel shows the ICNC dependence on w for a specific cloud base temperature (T), as labeled in each subplot. The different line styles distinguish the total ICNC ($N_{i,\mathrm{tot}}$, solid line), the contribution from dust nucleation ($N_{i,\mathrm{dust}}$, circle-dashed line), and the contribution from BC nucleation ($N_{i,\mathrm{BC}}$, cross-dotted line). All simulations were performed with fixed mass concentrations of 100 ng m^{-3} for both dust and BC, and background concentrations of 0.1 μg m^{-3} for both sea salt and sulfate at a cloud base pressure of 300 hPa.

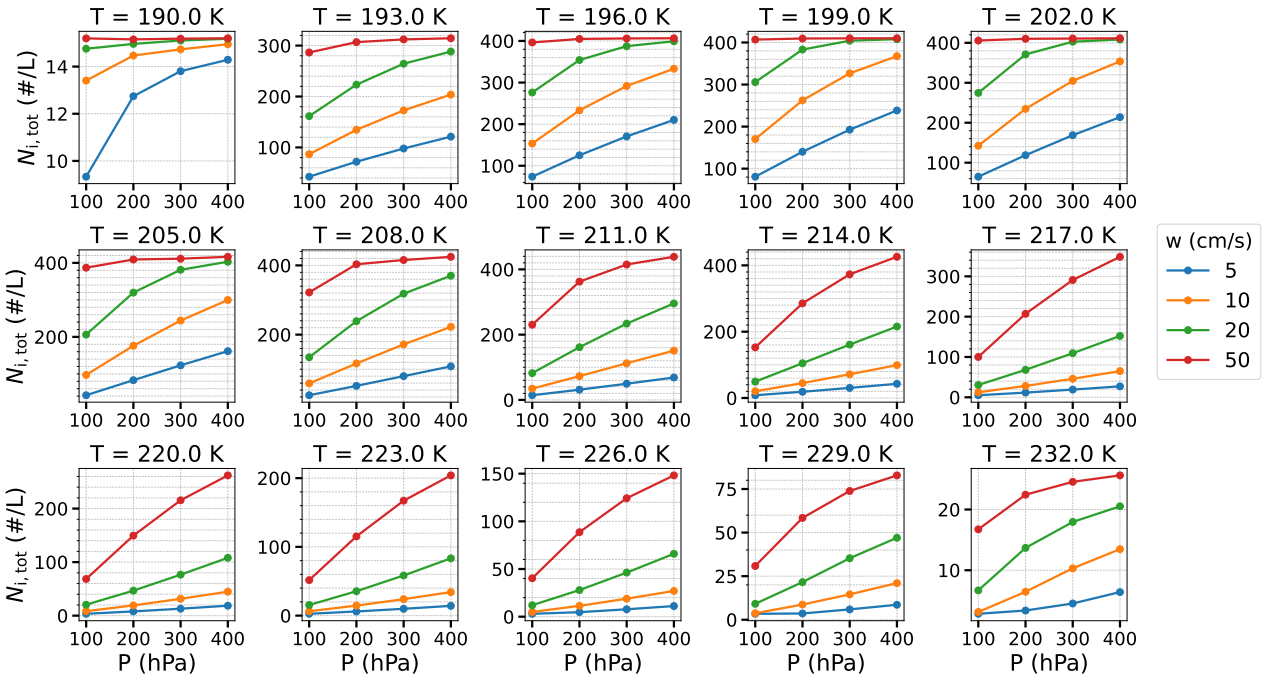

Figure S3. Total ice crystal number concentration ($N_{i,\mathrm{tot}}$) as a function of cloud base pressure (P). Each panel corresponds to a fixed cloud base temperature (T), as indicated in the subplot titles. Colored lines represent different updraft velocities (w). All simulations were performed with fixed mass concentrations of 100 ng m^{-3} for both dust and BC, and background concentrations of 0.1 μg m^{-3} for both sea salt and sulfate.

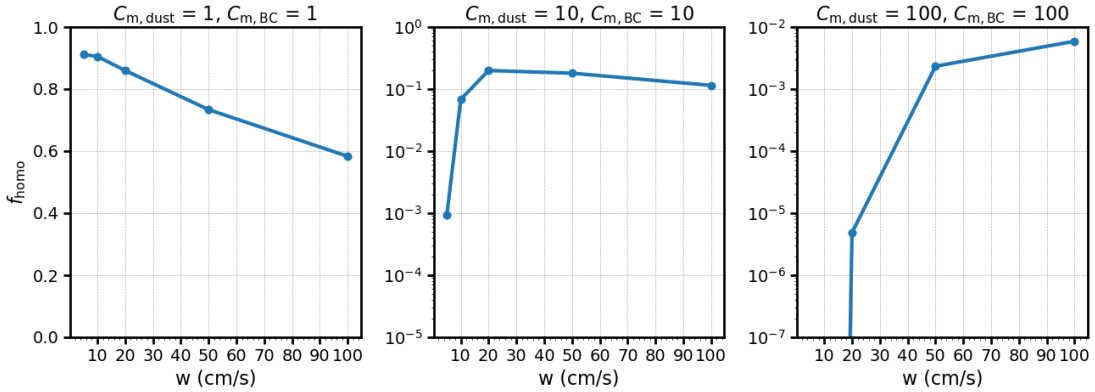

Figure S4. Fraction of ice crystals formed by homogeneous nucleation f_{homo} as a function of updraft velocity w for simulations with initial cloud base temperature of 232 K, cloud base pressure of 300 hPa, and background sulfate and sea-salt mass concentrations of 0.1 μg m^{-3}. Panels show different combinations of dust and BC mass concentrations ($C_{\mathrm{m,dust}}$ and $C_{\mathrm{m,BC}}$ in units of ng m^{-3}) from low to high (left to right). When dust and BC concentrations are low, homogeneous nucleation contributes up to more than 90% of the total ice crystals. The contribution decreases with increasing INP concentrations at the same updraft velocity, consistent with the expected suppression of homogeneous nucleation by heterogeneous nucleation on dust and BC.

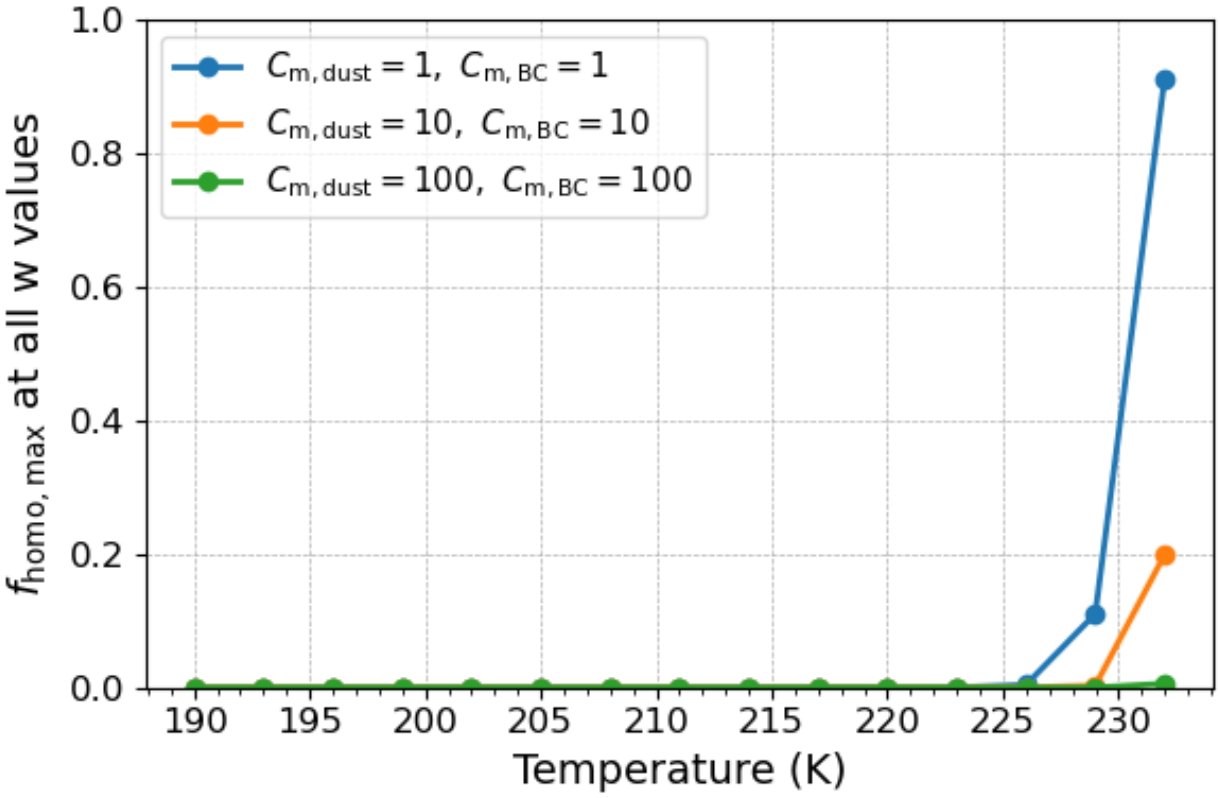

Figure S5. Maximum fraction of homogeneous ice crystals f_{homo} across all simulated updraft velocities as a function of temperature with initial cloud base temperature of 232 K, cloud base pressure of 300 hPa, and background sulfate and sea-salt mass concentrations of 0.1 μg m^{-3}. Homogeneous nucleation becomes important only at warmer temperatures ($T >\sim 230$ K), where the maximum value of f_{homo} can be substantial. At colder temperatures, the homogeneous fraction is negligible ($< 1\%$), reflecting strong depletion of supersaturation by heterogeneous nucleation on dust and BC. Different colored lines represent different combinations of dust and BC mass concentrations ($C_{\mathrm{m,dust}}$ and $C_{\mathrm{m,BC}}$ in units of ng m^{-3}).

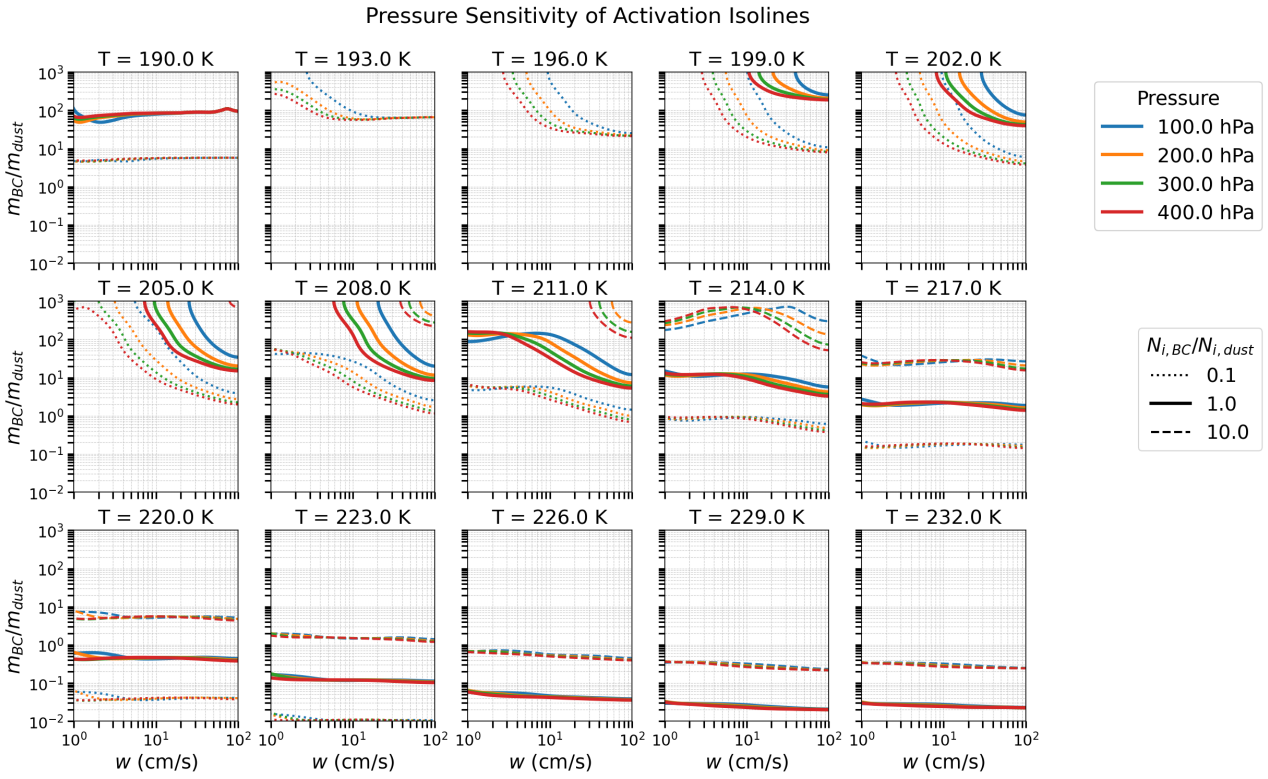

Figure S6. Sensitivity of the isolines of $N_{i,\mathrm{BC}}/N_{i,\mathrm{dust}}$ to meteorological conditions. Each subplot shows the ratio of BC-to-dust mass concentration ($m_{\mathrm{BC}}/m_{\mathrm{dust}}$) versus updraft velocity (w) at a different cloud base temperature T, as indicated in the subplot title. The lines represent isolines of $N_{i,\mathrm{BC}}/N_{i,\mathrm{dust}}$ equal to 0.1 (dotted), 1.0 (solid), and 10.0 (dashed). Different colors correspond to different cloud base pressures. All simulations assume fixed background concentrations of 0.1 μg m^{-3} for both sea salt and sulfate.

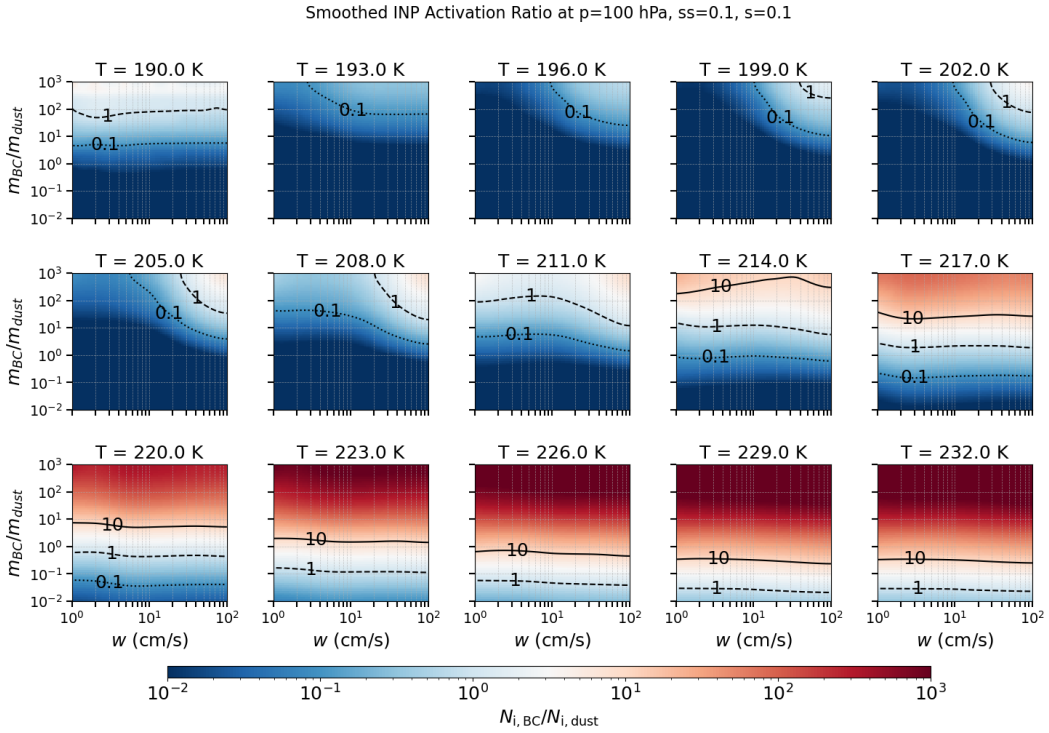

Figure S7. The relative importance of BC versus dust INPs, quantified by the ratio $N_{i,\mathrm{BC}}/N_{i,\mathrm{dust}}$ (color scale). The ratio is shown as a function of updraft velocity (w) and the initial aerosol mass ratio ($m_{\mathrm{BC}}/m_{\mathrm{dust}}$). Each panel corresponds to a different initial temperature from 190 K to 232 K. Isolines mark where the nucleation ratio is 0.1, 1, and 10. All simulations used a fixed pressure (100 hPa) and background aerosol (0.1 μg m^{-3} sea salt and sulfate).

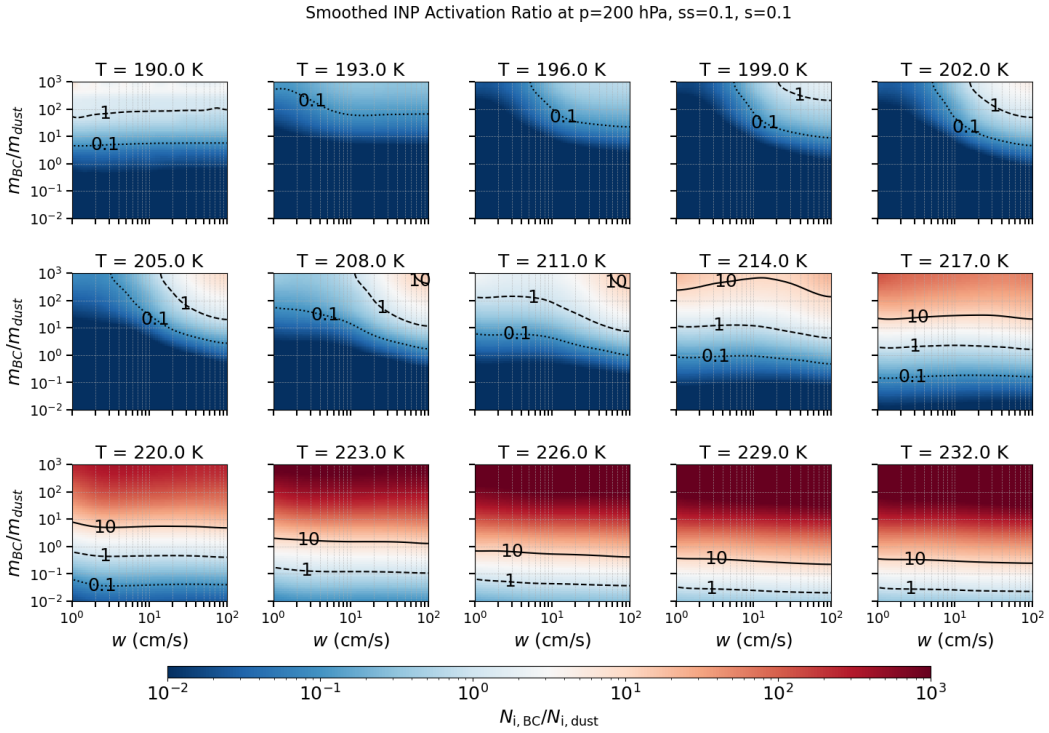

Figure S8. The relative importance of BC versus dust INPs, quantified by the ratio $N_{i,\mathrm{BC}}/N_{i,\mathrm{dust}}$ (color scale). The ratio is shown as a function of updraft velocity (w) and the initial aerosol mass ratio ($m_{\mathrm{BC}}/m_{\mathrm{dust}}$). Each panel corresponds to a different initial temperature from 190 K to 232 K. Isolines mark where the nucleation ratio is 0.1, 1, and 10. All simulations used a fixed pressure (200 hPa) and background aerosol (0.1 μg m^{-3} sea salt and sulfate).

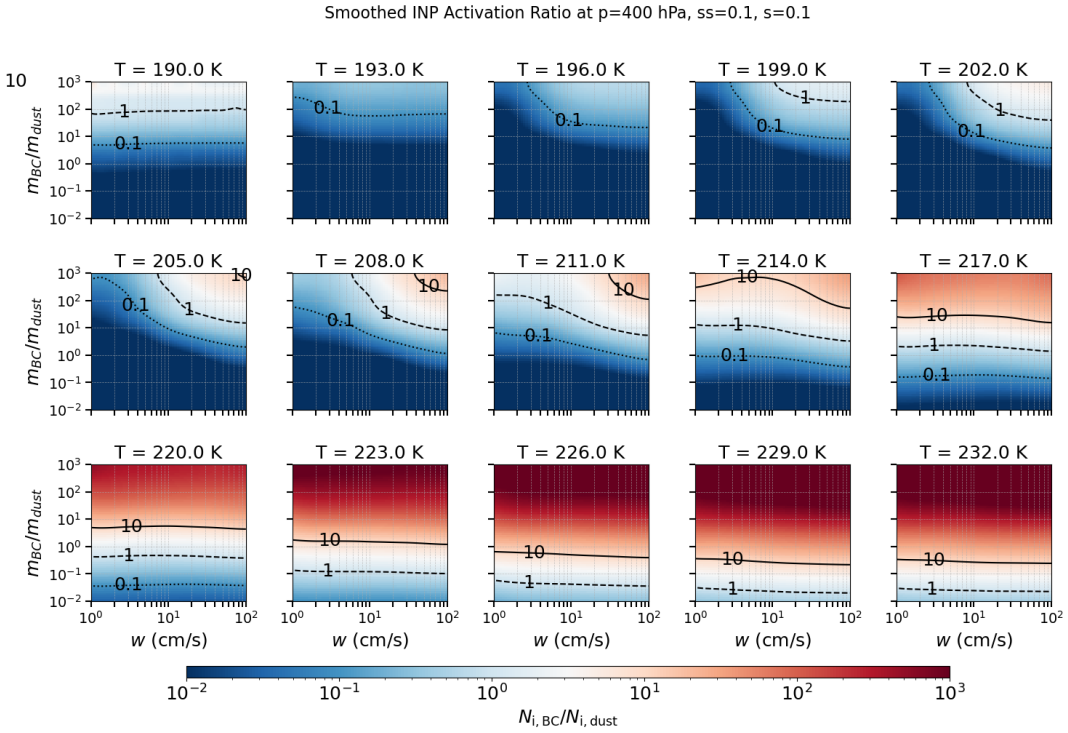

Figure S9. The relative importance of BC versus dust INPs, quantified by the ratio $N_{i,\mathrm{BC}}/N_{i,\mathrm{dust}}$ (color scale). The ratio is shown as a function of updraft velocity (w) and the initial aerosol mass ratio ($m_{\mathrm{BC}}/m_{\mathrm{dust}}$). Each panel corresponds to a different initial temperature from 190 K to 232 K. Isolines mark where the nucleation ratio is 0.1, 1, and 10. All simulations used a fixed pressure (400 hPa) and background aerosol (0.1 μg m^{-3} sea salt and sulfate).

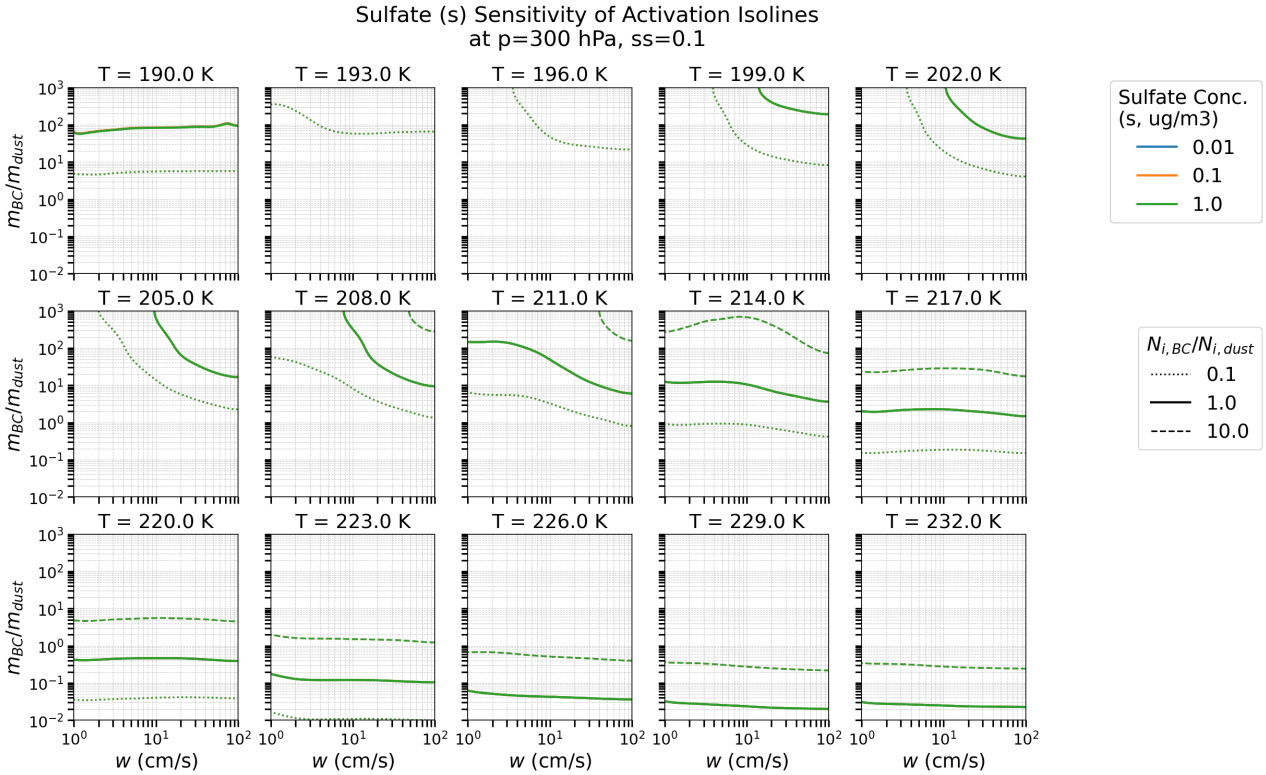

Figure S10. Sensitivity of the isolines of $N_{i,\mathrm{BC}}/N_{i,\mathrm{dust}}$ to sulfate concentration. Each subplot shows the ratio of BC-to-dust mass concentration ($m_{\mathrm{BC}}/m_{\mathrm{dust}}$) versus updraft velocity (w) at a different cloud base temperature T, as indicated in the subplot title. The lines represent isolines of $N_{i,\mathrm{BC}}/N_{i,\mathrm{dust}}$ equal to 0.1 (dotted), 1.0 (solid), and 10.0 (dashed). Different colors correspond to different sulfate concentrations. All simulations assume fixed background concentrations of 0.1 μg m^{-3} for sea salt, dust, and BC. We note that the isolines are shown in green for all cases, as they overlap across different sulfate levels.

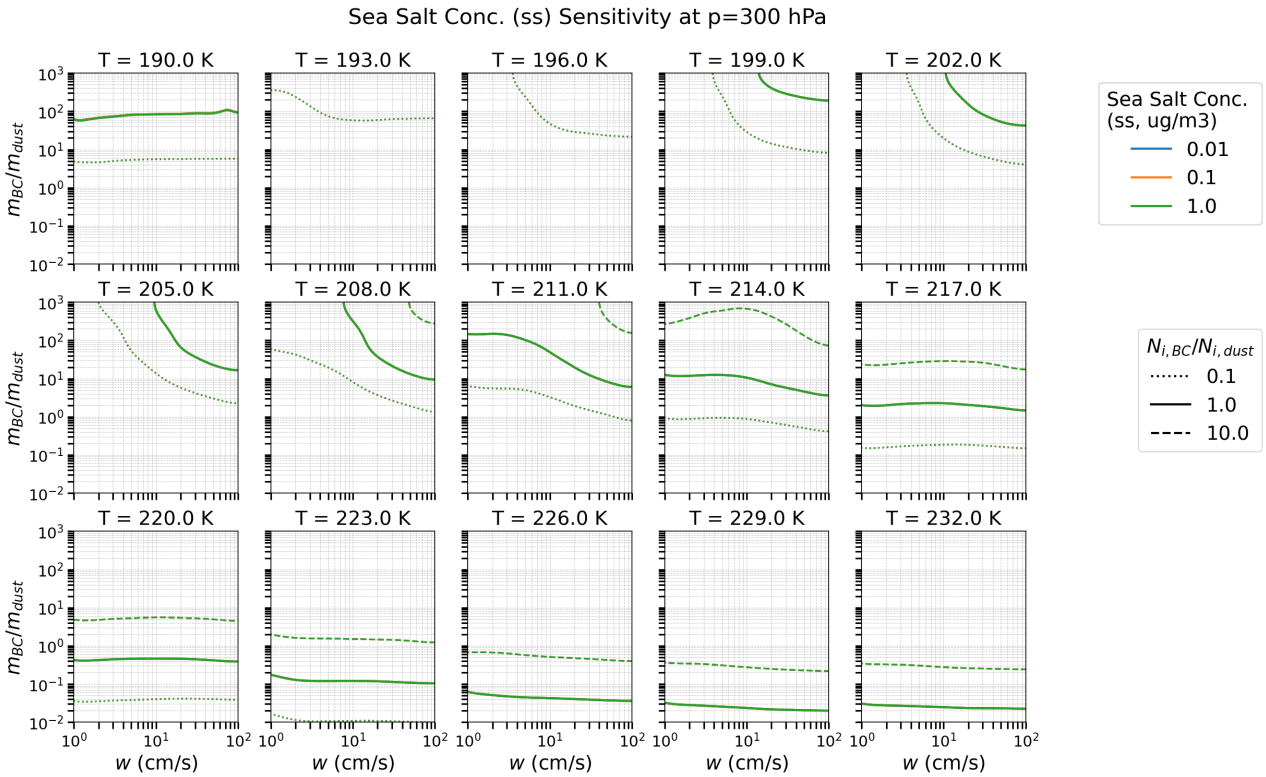

Figure S11. Sensitivity of the isolines of $N_{i,\mathrm{BC}}/N_{i,\mathrm{dust}}$ to seas salt concentration. Each subplot shows the ratio of BC-to-dust mass concentration ($m_{\mathrm{BC}}/m_{\mathrm{dust}}$) versus updraft velocity (w) at a different cloud base temperature T, as indicated in the subplot title. The lines represent isolines of $N_{i,\mathrm{BC}}/N_{i,\mathrm{dust}}$ equal to 0.1 (dotted), 1.0 (solid), and 10.0 (dashed). Different colors correspond to different sea salt concentrations. All simulations assume fixed background concentrations of 0.1 μg m^{-3} for sulfate, dust, and BC. We note that the isolines are shown in green for all cases, as they overlap across different sea salt levels.

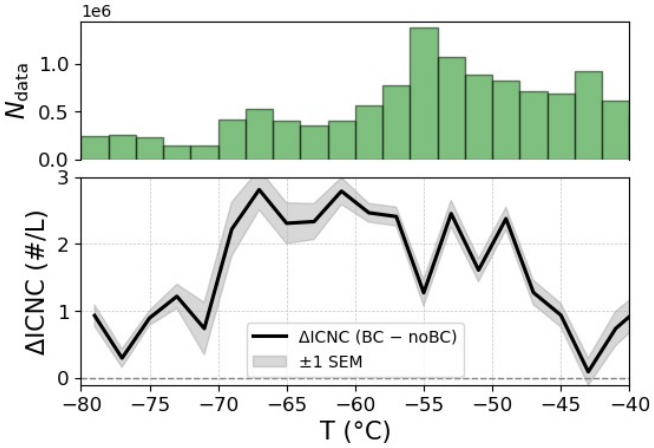

Figure S12. Difference in ICNC (ΔICNC) between GCM simulations with and without BC acting as INPs. The shaded region represents the standard error of the mean (SEM) of the difference. The top panel above shows the data count distribution versus temperature from the simulation that includes BC; the distribution for the no-BC case is omitted as it is nearly identical with the BC case.

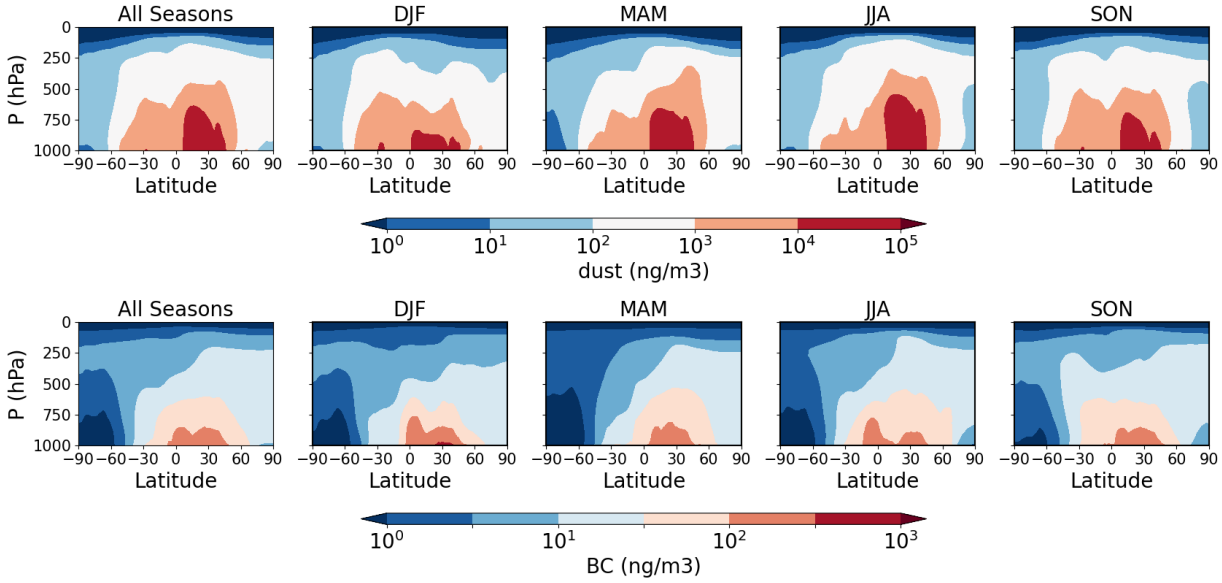

Figure S13. Seasonal zonal mean distributions of dust and black carbon (BC) mass concentration. The upper row of panels shows the mass concentration for dust, while the lower row shows the mass concentration for BC. Each column represents a different season.

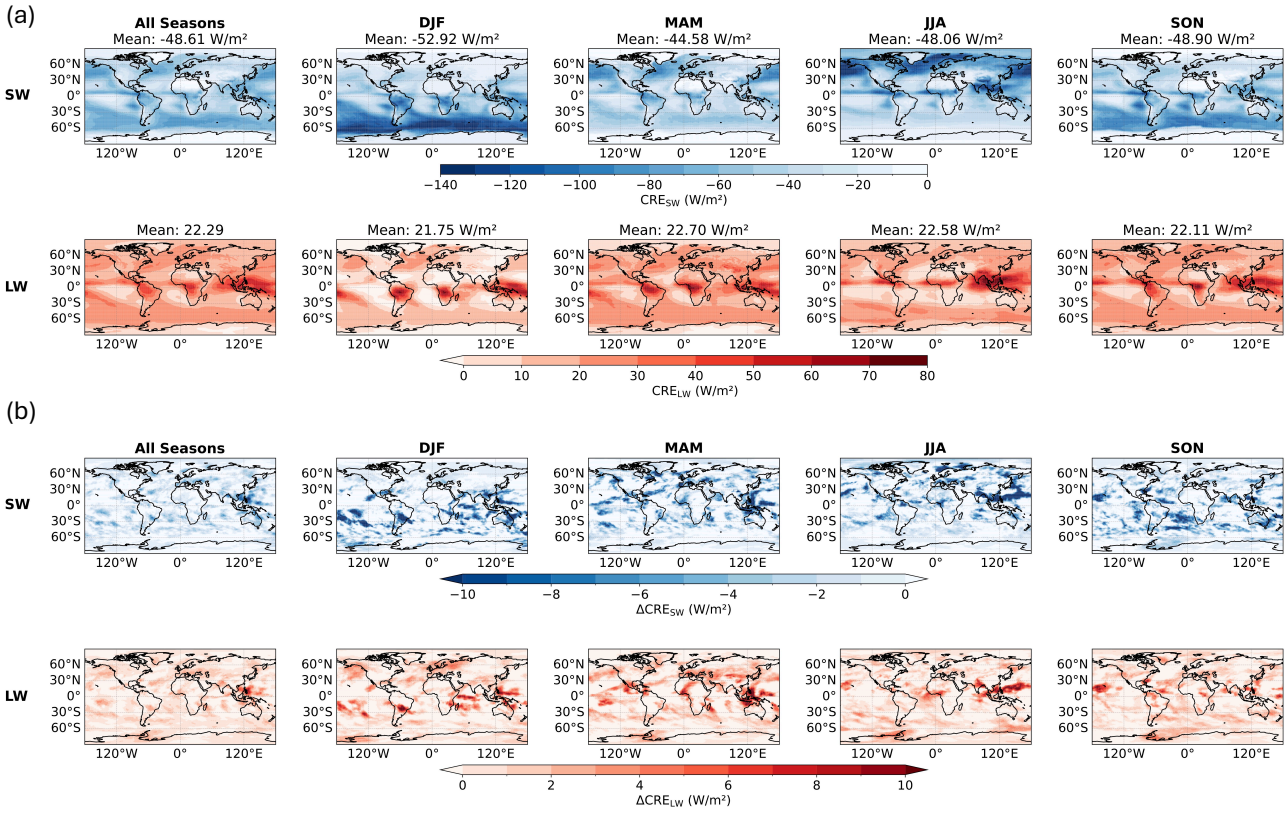

Figure S14. Cloud Radiative Effect (CRE) and its response to BC as INPs at the top of the atmosphere (TOA) computed over 2001–2005. **(a)** Seasonal mean shortwave (CRE_{SW}, upper panel) and longwave (CRE_{LW}, lower panel) cloud radiative effects from simulations that include BC INPs. Negative values (blue) indicate a net cooling effect by clouds, while positive values (red) indicate a net warming effect. **(b)** The difference in CRE (ΔCRE) caused by BC INPs, calculated as the difference between simulations with and without BC ($\Delta CRE = CRE_{BC} - CRE_{noBC}$). The upper and lower panels show the shortwave (ΔCRE_{SW}) and longwave (ΔCRE_{LW}) components, respectively. Here, negative values signify that BC enhances radiative cooling, while positive values signify an enhancement of radiative warming.

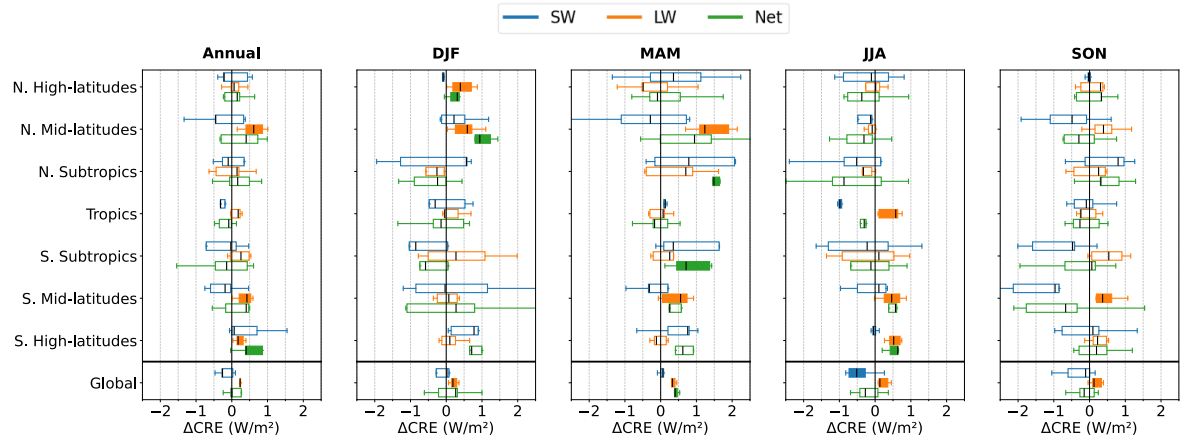

Figure S15. Cloud Radiative Effect (CRE) and its response to BC as INPs at the top of the atmosphere (TOA) computed over 2001–2005. Box plots of annual and seasonal ΔCRE across different latitudinal regions, spatially averaged within each region and computed over a 5-year period. The regions shown are the N. High-latitudes (60°N–90°N), N. Mid-latitudes (35°N–60°N), N. Subtropics (23.5°N–35°N), Tropics (23.5°S–23.5°N), S. Subtropics (23.5°S–35°S), S. Mid-latitudes (35°S–60°S), S. High-latitudes (60°S–90°S), and the Global mean. Filled boxplots indicate that the mean ΔCRE is statistically significant different from 0 ($p < 0.05$).

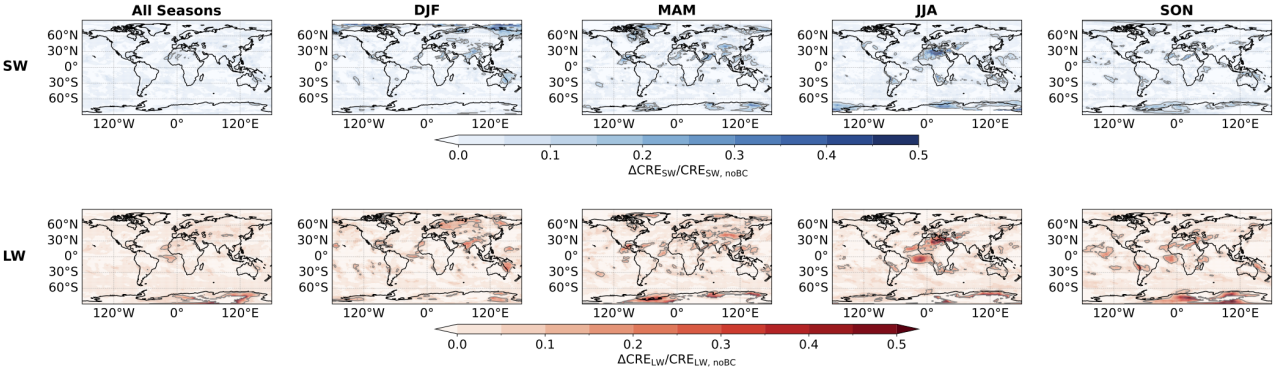

Figure S16. The relative change in cloud radiative effect (CRE) due to BC INPs, expressed as $\Delta CRE/CRE_{noBC}$ averaged over 2001-2020. The upper and lower panels show the shortwave ($\Delta CRE_{SW}/CRE_{noBC,SW}$) and longwave ($\Delta CRE_{LW}/CRE_{noBC,LW}$) components, respectively. Isolines indicate enhancement fractions equal to 0.1.

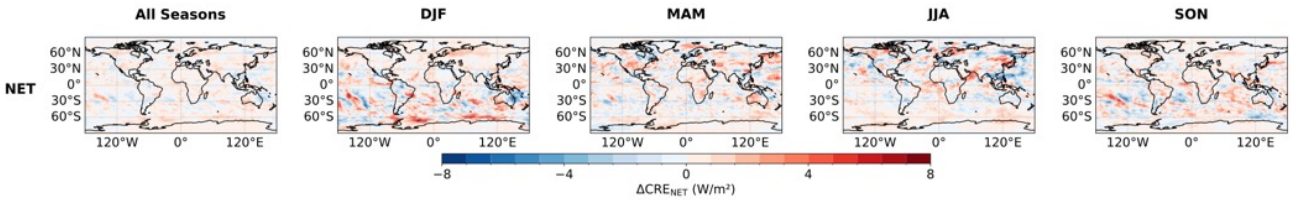

Figure S17. The spatial distribution of the net cloud radiative effect (ΔCRE_{net}) induced by BC INPs averaged over 2001-2020. Results are shown for the annual mean and for different seasons. Positive values indicate that the longwave (LW) warming effect dominates the shortwave (SW) cooling effect.

References

Alpert, P. A. and Knopf, D. A.: Analysis of isothermal and cooling-rate-dependent immersion freezing by a unifying stochastic ice nucleation model, Atmospheric Chemistry and Physics, 16, 2083–2107, 2016.

Koop, T., Luo, B., Tsias, A., and Peter, T.: Water activity as the determinant for homogeneous ice nucleation in aqueous solutions, Nature, 406, 611–614, 2000.

Pruppacher, H. R., Klett, J. D., and Wang, P. K.: Microphysics of clouds and precipitation, 1998.

Ullrich, R., Hoose, C., Möhler, O., Niemand, M., Wagner, R., Höhler, K., Hiranuma, N., Saathoff, H., and Leisner, T.: A new ice nucleation active site parameterization for desert dust and soot, Journal of the Atmospheric Sciences, 74, 699–717, 2017.

Ullrich, R., Hoose, C., Cziczo, D. J., Froyd, K. D., Schwarz, J. P., Perring, A. E., Bui, T. V., Schmitt, C. G., Vogel, B., Rieger, D., et al.: Comparison of modeled and measured ice nucleating particle composition in a cirrus cloud, Journal of the Atmospheric Sciences, 76, 1015–1029, 2019.